ORIGINAL RESEARCH ARTICLE

Deconstructing the Retained Austenite Stability: A Comparative Study of Two-Phase and Bulk Microstructures

JOSHUA KUMPATI, SK.MD. HASAN, MANON BONVALET ROLLAND, and ANNIKA BORGENSTAM

The stability of retained austenite is a key factor in the design of advanced high-strength steels that exhibit excellent mechanical performance, including high strength and high ductility/toughness. However, the contribution of certain microstructural factors, such as the morphology and size of the austenite, and the surrounding matrix, to this stability is still not fully understood, partly due to the inherent difficulties in separating these factors in multiphase microstructures. Therefore, this study uniquely compared the stabilities of retained austenite in two-phase microstructures with bulk austenitic microstructures of the same composition, across four medium-Mn steels upon quenching. By fixing the austenite chemical composition, we could exclude the influence of composition and examine the influence of other factors, such as morphology, size, and the surrounding matrix, on the stability of austenite. Our experimental results showed that retained austenite in the two-phase microstructures was more stable than the bulk austenitic microstructures of the same composition, regardless of morphology and size. Analysis using thermodynamic calculations revealed that neither the steel composition nor the size alone could explain the high stability of the retained austenite in the two-phase microstructures. Instead, we propose that microstructural factors, including size, morphology, and matrix, have a significant influence on the metastable austenite in two-phase microstructures. While these factors have been studied previously, our study introduces a novel perspective by excluding the influence of the austenite composition, thus contributing to a more comprehensive understanding of retained austenite stability. These findings may guide the design of advanced steels and highlight the importance of considering the contribution of these microstructural factors in tailoring the stability of metastable austenite.

https://doi.org/10.1007/s11661-023-07258-8

I. INTRODUCTION

CONTINUOUS development in the area of steel technology has led us from the first generation of advanced high-strength steels (AHSS), which include dual-phase (DP), transformation-induced plasticity (TRIP), complex phase (CP), and martensitic (M) steels to the second generation of AHSS, *e.g.* twinning induced plasticity (TWIP) steels.[1,2] In recent times, there has been an increased interest in the development of the third generation of AHSS with a much-improved combination of strength and ductility/toughness and reduced cost.[3,4] Quenching and partitioning (Q&P) steels,[5] medium Mn steels,[6,7] nanostructured and carbide-free bainitic steels[8,9] are some examples of the third-generation of AHSS. These steels consist of a high-strength microstructure (*e.g.* ultrafine-grained ferrite/martensite/bainite) and/or a significant amount of retained austenite (RA) that improves the work hardening of the multi-phase structure by a TRIP effect.[10,11] The stability of RA, generally described in terms of thermal and mechanical stability plays a crucial role in determining the mechanical properties of these steels.[12,13] This manuscript focuses on the thermal driving force instead of a mechanical driving force due to an applied load, specifically examining the austenite

JOSHUA KUMPATI and ANNIKA BORGENSTAM are with the Department of Materials Science and Engineering, KTH Royal Institute of Technology, 10044 Stockholm, Sweden. Contact e-mail: joshva@kth.se SK. MD. HASAN is with the Department of Materials Science and Engineering, KTH Royal Institute of Technology and also with the Department of Metallurgical and Materials Engineering, Indian Institute of Technology, Jodhpur, Jodhpur 342037, India. MANON BONVALET ROLLAND is with the Department of Materials Science and Engineering, KTH Royal Institute of Technology and also with the Univ. Lille, CNRS, INRAE, Centrale Lille, UMR 8207 – UMET – Unité Matériaux et Transformations, 59000 Lille, France.
Manuscript submitted June 2, 2023; accepted November 9, 2023.
Article published online November 23, 2023

(γ) $\rightarrow$ α'-martensite transformation. The thermal stability of γ refers to its ability to remain untransformed (*i.e.*, resistance to the formation of α'-martensite) during treatments involving temperature changes and is usually quantified using the martensite start temperature (M_s). Several factors, including temperature, chemical composition, size, orientation, and morphology, can influence thermal stability.[12,14–16]

In general, smaller γ grains tend to be more stable and thus have lower M_s temperatures than larger γ grains.[4,17] The influence of grain size on the thermal stability of γ has been explained by several theories from different perspectives based on the inhibition effect it has on the $\gamma \rightarrow \alpha'$ transformation.[18–20] Although researchers have reported a critical γ grain size of 15 to 25 μm above which M_s does not show significant variation with the grain size,[21–23] it should be noted that a significant change in M_s has been observed in previous studies for grain sizes below this critical size, increasing in the submicron range.[23,24] It has also been suggested that the formation of multivariant martensite is significantly reduced or even suppressed below this critical γ grain size, resulting in more difficult accommodation of plastic strain associated with $\gamma \rightarrow \alpha'$ transformation.[18,25] Furthermore, the γ grain size dependency of M_s is not linear, and several empirical/semi-empirical expressions have been proposed to take into account the effect of γ grain size on the M_s temperature.[4,21,23,26]

The role of dislocations in the stability of austenite is complex and often contradictory. Despite numerous studies in this area, the exact influence of dislocations on austenite stability remains ambiguously defined due to their potential role in facilitating or hindering martensitic transformation. Under certain conditions, such as when a small number of dislocations ($\sim 10^{13}$ to 10^{14} m^{-2}) exist within the austenite structure, these dislocations can facilitate martensitic transformation by directly influencing the nucleation and growth stages.[27] On the other hand, when there are a large number of dislocations ($> 10^{16}$ m^{-2}), they can act as barriers, inhibiting martensite growth.

Blocky (γ_b) and thin film (γ_f) are the two commonly distinguished morphologies of RA, in AHSS.[4,12] It has been observed experimentally that γ_f is more stable than γ_b in different steel grades.[14,28–30] Several additional factors, such as carbon content,[14] size (volume),[4] dislocation density,[13,29] and hydrostatic pressure (leading to the shielding effect)[31] have been shown to contribute to the enhanced thermal stability of γ_f. Moreover, a great deal of work has been carried out to address the stability of γ as a function of its morphology in AHSS.[14,31–33] However, these investigations could not reasonably delineate the effective contribution of morphology to the stability of γ. For example, the content of carbon and other alloying elements, which is dependent on processing conditions, is typically higher in blocks or thin films of RA compared to the parent γ. Additionally, the carbon content can vary between blocks or thin films of γ and the relative stability of γ in such cases will thus be affected by a combination of the morphology and its chemical composition, which the existing literature could not distinguish due to insufficient information.

The current study aims to investigate the role of different microstructural factors by comparing microstructures with different RA morphologies ($\alpha' + \gamma_f$ or $\alpha' + \gamma_b/\gamma_f$) and bulk γ microstructures of the same composition as the RA, across four medium-Mn steels. This approach will help separate the influence of chemical composition on the stability of RA and examine the contribution of other factors. Accordingly in this work, the thermal stability of different microstructures was experimentally studied using a combination of scanning electron microscopy (SEM), electron backscatter diffraction (EBSD), X-ray diffraction (XRD), and dilatometry techniques, and predictions from a thermodynamic-based M_s model were compared with experimental results.

II. METHODOLOGY

A. *Materials and Heat Treatments*

The chemical compositions of the four medium-Mn steels used in this work are listed in Table I. These four steels were subjected to different heat treatment cycles to produce the desired microstructures. The aim for two of the steels was to create a two-phase microstructure with a martensitic matrix and γ of a particular morphology: thin film, Steel 1, or blocky, Steel 3. The aim for the two others, Steel 2 and Steel 4 was to create a bulk microstructure consisting entirely of γ before quenching after the last heat treatment with the same composition as the RA in Steels 1 and 3, respectively. These four steels are grouped into two pairs (each pair includes a two-phase and a corresponding bulk γ microstructure) to investigate the role of morphology and surrounding matrix on γ stability. All samples were cut from an 8 mm thick hot-rolled steel plate, except Steel 2 which was cut from an as-cast material. During heat treatment, the samples were encapsulated in quartz tubes to prevent oxidation from the surrounding atmosphere.

The heat treatment processes applied to the four steels are summarized in Figure 1. Steel 1, Figure 1(a), was homogenized at 1200 °C for 15 hours and water quenched to room temperature. It was then austenitized at 900 °C for 15 minutes before being water quenched to room temperature to form a fully martensitic microstructure. Subsequently, it was intercritically annealed (IA) at 650 °C for 3 hours to create a two-phase microstructure consisting of a martensitic matrix and γ_f, followed by water quenching to room temperature. Steel 2, Figure 1(b), was homogenized at 1250 °C for 48 hours and water quenched to room temperature and was subsequently cooled using liquid nitrogen to have a fully martensitic microstructure as the other steels before the heat treatment. It was then austenitized at 900 °C for 15 minutes followed by water quenching to room temperature. Steel 3, Figure 1(c), was homogenized at 1250 °C for 24 hours, followed by water quenching to room temperature. It was then processed using a Quenching and Partitioning (Q&P)

Table I. Chemical Composition of the Four Medium Mn Steels (in Weight Percent)

Material	C	Mn	Si	Cr	Fe	Targeted Microstructure at Austenitization/IA/Q&P
Steel 1	0.18	5.08	—	—	bal.	two-phase ($\alpha' + \gamma_f$)
Steel 2	0.68	7.31	—	—	bal.	one-phase (γ)
Steel 3	0.31	4.02	1.62	1.01	bal.	two-phase ($\alpha' + \gamma_b$)
Steel 4	0.56	4.01	1.63	1.01	bal.	one-phase (γ)

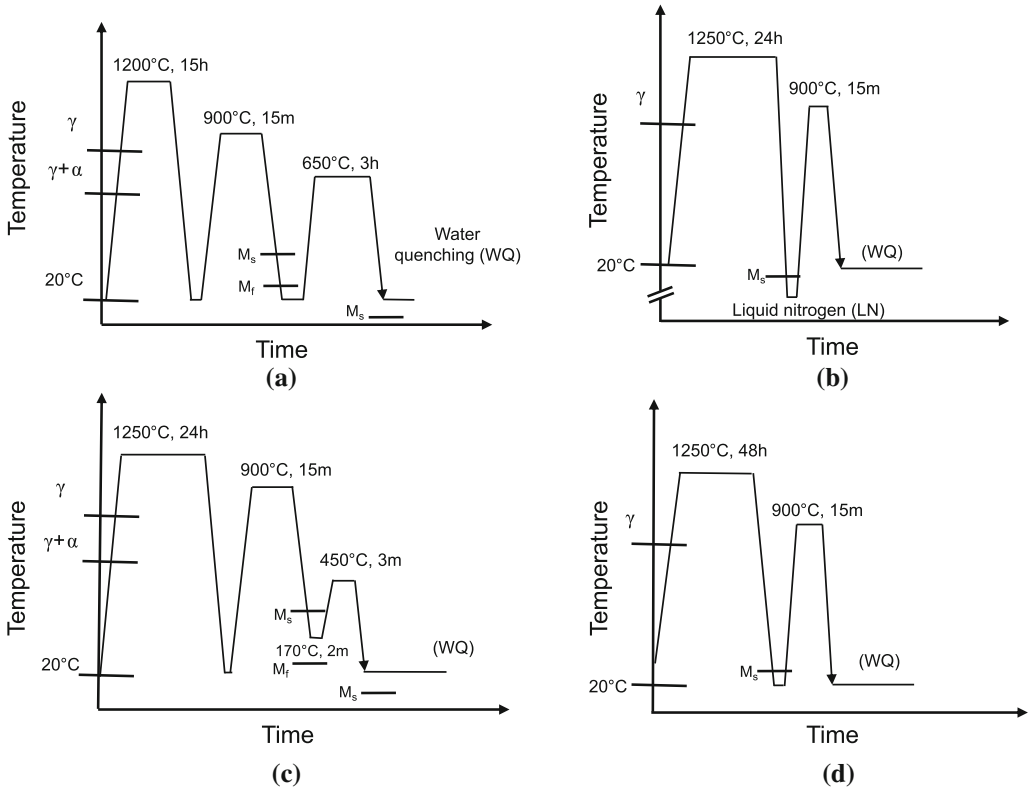

Fig. 1—Schematic representation of the heat treatment cycles for the four steels. (*a*) Steel 1, (*b*) Steel 2, (*c*) Steel 3, (*d*) Steel 4.

heat treatment to produce a two-phase microstructure consisting of a martensitic matrix and γ_b. The Q&P process was performed using a combination of a box furnace and salt baths. It was fully austenitized at 900 °C for 15 minutes and initially cooled to a quenching temperature (QT) of 170 °C for the γ to partially transform into martensite. It was held at this temperature for 2 minutes to ensure a uniform temperature throughout the sample and then reheated to a partitioning temperature (PT) of 450 °C for 3 minutes, and finally, water quenched to room temperature. Finally, Steel 4, Figure 1(d), was homogenized at 1250 °C for 48 hours, and water quenched to room temperature. The steel was reaustenitized at 900 °C for 15 minutes before finally water quenched to room temperature.

B. *Microstructural Characterization*

The characterization and quantification of the microstructures of the four medium Mn steels were done using SEM, EBSD, XRD, and dilatometry. All samples were mechanically ground and polished down to 1 μm step. Samples for SEM studies were etched in Nital-2 pct in ethanol for 5 seconds, while samples for EBSD had an additional polishing step using a colloidal silica suspension (0.02 μm) to obtain a good surface finish. For XRD analysis, a final electrochemical polishing in a solution of 10 volume pct $HClO_4$–ethanol was performed to remove any possible mechanically induced martensite from the prior polishing steps.

The SEM used in the present study was a field emission gun scanning electron microscope (FEG-SEM JEOL JSM-7800F), operated at 15 kV and a working distance of about 10 mm. EBSD mappings were recorded with a FEI Nova Nano Lab 600 dual beam equipped with an Oxford EBSD detector using an accelerating voltage of 20 kV with varying beam current and a working distance of 10 mm. The EBSD data was post-processed with AZtecCrystal software.

XRD measurements were performed on a Bruker D8 advanced diffractometer with Cu-Kα radiation to determine the amount of RA and its average carbon content.

The scanned 2θ range was 40 to 100 deg with a step size of 0.02 deg and a measurement time of 3 seconds per step. The amount of different constituent phases was determined using the direct comparison method.[34] This method correlates the volume fraction of all phases present in the microstructure with the integrated intensity as follows

$$f_i = \frac{\frac{1}{n}\sum_{j=1}^{n}\frac{I_i^j}{R_i^j}}{\frac{1}{n}\sum_{j=1}^{n}\frac{I_\gamma^j}{R_\gamma^j}+\frac{1}{n}\sum_{j=1}^{n}\frac{I_{\alpha'}^j}{R_{\alpha'}^j}+\frac{1}{n}\sum_{j=1}^{n}\frac{I_\varepsilon^j}{R_\varepsilon^j}} \quad [1]$$

where n is the number of peaks examined for a particular phase i, and f_i, I_i and R_i are respectively the volume fraction, integrated intensity, and crystal structure parameter. The lattice parameter of γ (a_γ) after final quenching was determined by the Nelson-Riley method[34] and was converted to the γ carbon content (in wt pct) using the following empirical relationships given by[35–37].

$$\alpha_\gamma(\text{Å}) = 3.556 + 0.0453w_C + 0.00095w_{Mn} + 0.0006w_{Cr} \quad \text{(Two-phase)} \quad [2]$$

$$\alpha_\gamma(\text{Å}) = 3.578 + 0.033w_C + 0.00095w_{Mn} + 0.0006w_{Cr} \quad \text{(Bulk)} \quad [3]$$

where the concentration w_i of the alloying elements 'i' is in wt pct. Equation [2] correlates the RA lattice parameter to alloying elements accounting for the influence of a martensitic matrix while Eq. [3] correlates the γ lattice parameter with the alloying elements in the absence of a martensitic matrix and is valid for bulk γ microstructures. The influence of Si on the lattice parameter of γ was found to be negligible within the experimental accuracy.[28] Average dislocation density of the different phases in each steel has been estimated from the respective XRD peaks using the Williamson-Hall method.[38]

Dilatometric investigations were performed in a Bähr 805 dilatometer under vacuum. Cylindrical hollow specimens of 10 mm length, 4 mm external diameter, and 3 mm internal diameter were machined using electrical wire discharging. Nitrogen or/and helium gas were used as the quenching medium during the experiments. The M_s temperature was determined from the dilatometry data using the offset method.[39]

III. RESULTS

A. *Steel 1: Microstructure and RA (Thin Film) Stability*

Dilatometer results on Steel 1, as shown in Figure 2(a), indicate that the material was fully austenitized during the initial austenitization heat treatment at 900 °C. The M_s temperature of the bulk γ was determined to 284 °C ± 5 °C. The dilatometry results show that the transformation of γ into α'-martensite is completed above room temperature, resulting in a fully martensitic microstructure at room temperature before IA. However, these results show that the γ formed during IA remains stable during subsequent cooling to − 100 °C, as indicated by the insignificant deviation from the linear contraction of the γ during cooling, see Figure 2(a). This shows that the γ at the end of the IA step is stable at RT and has a M_s below − 100 °C.

XRD measurements at room temperature after IA and quenching to RT reveals the presence of RA (fcc) and α'-martensite (bcc), with volume fractions of 0.29 ± 0.03 and 0.71 ± 0.03, respectively, see Figure 3. Further, after quenching in liquid nitrogen (LN) XRD shows a similar amount of RA as at room temperature, Figure 4, indicating that the RA did not undergo any significant martensitic transformation even at temperatures down to as low as − 196 °C, indicating very high stability of the RA. Based on these room temperature XRD measurements, the dislocation densities were also evaluated and determined to be 2.7369×10^{15} m^{-2} and 1.0271×10^{15} m^{-2} for the RA and α'-martensite, respectively, as shown in Table II.

The SEM micrograph in Figure 5(a) reveals the two-phase microstructure of Steel 1 after IA and quenching to room temperature, consisting of a martensitic matrix and ultrafine RA. The RA is predominantly located between the martensite laths and is mainly in the form of thin films with an average thickness of approximately 0.6 μm. The EBSD analysis of Steel 1 is shown in Figure 5(b), which includes a combined image quality (IQ) map and a color-coded phase map. RA (red) α'-martensite (blue) phases are identified by EBSD. The volume fraction of RA and α'-martensite obtained from EBSD are 0.25 and 0.72, respectively. The XRD analysis, Figure 3, indicated a similar volume fraction of RA (0.29 ± 0.03) which is within the experimental uncertainty. The average composition of the RA at the end of IA is 0.69C–7.3Mn, determined in previous work[4] using a combination of transmission electron microscopy-energy dispersive X-ray spectroscopy (TEM-EDX) and XRD techniques.

B. *Steel 2: Microstructure and γ (Bulk) Stability*

Dilatometer results, shown in Figure 2(b), indicate that Steel 2 was fully austenitized when heated to 900 °C. The M_s temperature was determined to − 8 °C ± 5 °C, showing that γ remains metastable at room temperature. The microstructure of Steel 2 at RT, observed by SEM [Figure 5(c)], consists mainly of equiaxed γ grains with an average size of approximately 35 μm. Some γ grains also exhibit annealing twins, and a few contain thin parallel lines of ε-martensite and a small fraction of α'-martensite. The observed α'-martensite in the microstructure is probably the result of deformation-induced transformation, which is in this case supported by the dilatometer results indicating a M_s temperature of − 8 °C for α'-martensite. Also, the ε-martensite transformation is associated with a volume contraction in the specimen, however, no detectable volume contraction was observed in the dilatometer measurement, most likely due to the low fraction of

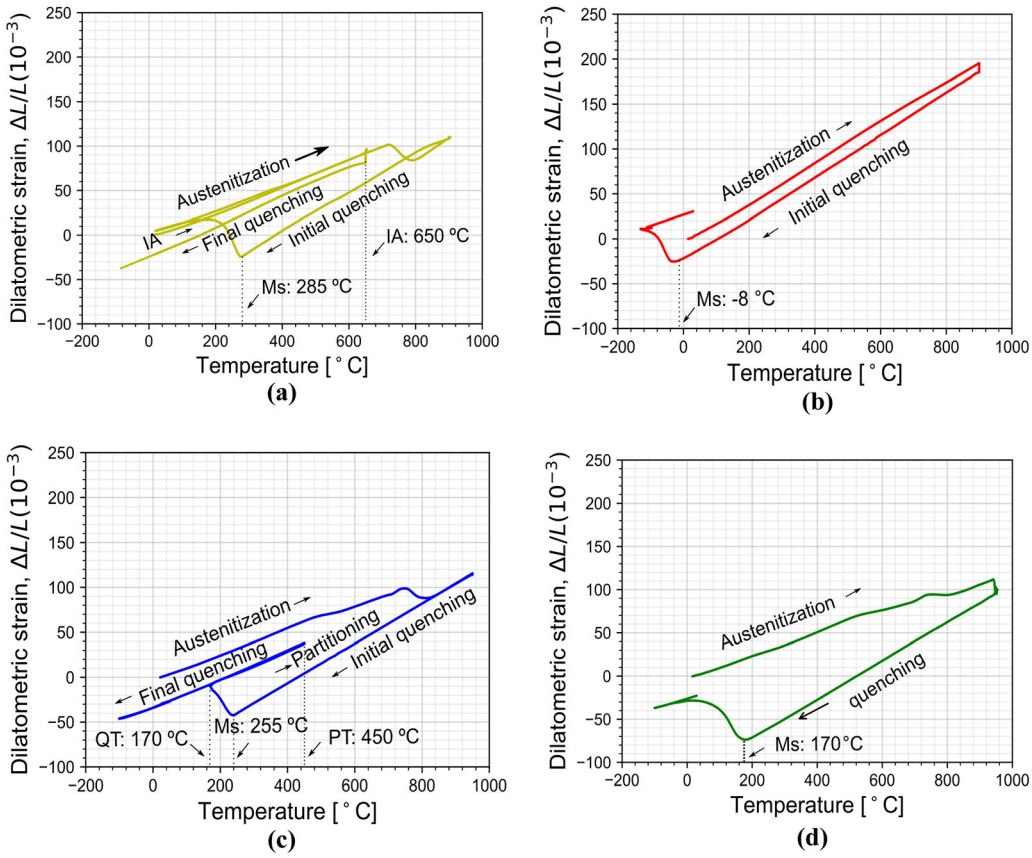

Fig. 2—Dilatometry strains of the four steels for their respective heat treatments. (*a*) Steel 1, (*b*) Steel 2, (*c*) Steel 3, and (*d*) Steel 4. The M_s temperatures determined from the dilatometry measurements are indicated.

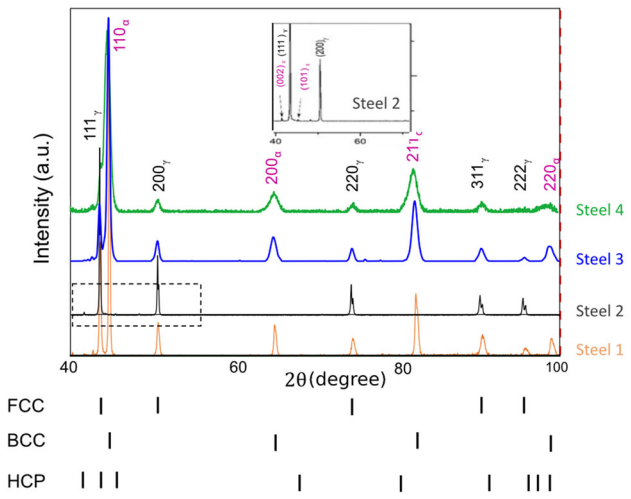

Fig. 3—Room temperature XRD patterns of the four steels after heat treatment. The patterns reveal the presence of different phases in each steel, with the inset of Steel 2 highlighting the presence of ε-martensite peaks. It should be noted that the double peaks observed in Steel 2 are due to the Cu-Kα2 radiation.

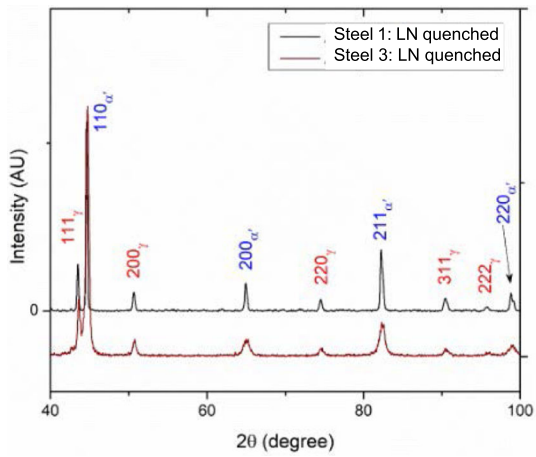

Fig. 4—XRD patterns of Steel 1 and 3 after quenching in liquid nitrogen where the peaks corresponding to RA are still visible, indicating its stability in the two-phase microstructures.

ε-martensite formed and thus that the $\gamma \rightarrow \varepsilon$ transformation start temperature could not be determined in the present case.

XRD analysis, Figure 3, reveals the presence of γ (fcc) and ε-martensite (hcp) at room temperature, with volume fractions of 0.97 ± 0.03 and 0.03 ± 0.03, respectively. Notably, the XRD measurements did not detect the presence of any bcc phase, *i.e.*, α′-martensite. The α′-martensite which in this steel probably is deformation induced is thus limited to the sample's surface and subsequently removed during the electropolishing step. The EBSD analysis, Figure 5(d), shows a volume fraction of 0.98 RA. α′-martensite (blue) was also

Table II. Dislocation Densities of the Four Steels Measured at Room Temperature

Sample	Dislocation Density, ρ (m^{-2})	
	$\rho_{martensite}$	$\rho_{austenite}$
Steel 1	1.0271×10^{15}	2.7369×10^{15}
Steel 2	—	5.7805×10^{14}
Steel 3	4.5274×10^{15}	5.9722×10^{15}
Steel 4	2.729×10^{16}	8.937×10^{15}

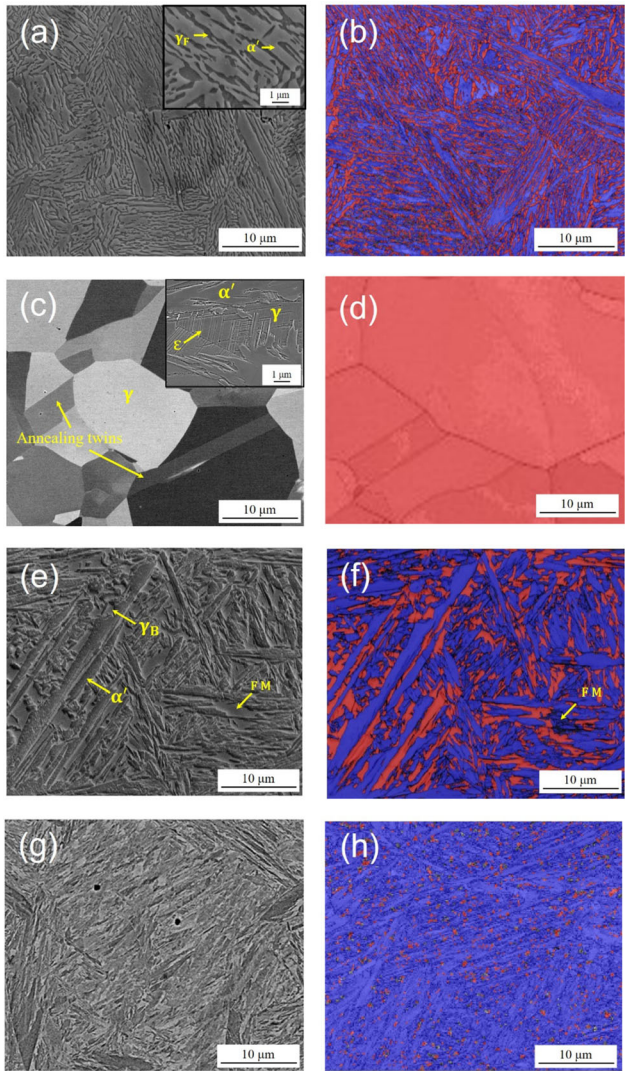

Fig. 5—SEM micrographs and EBSD combined image quality (IQ) map and color-coded phase images of the four steels after their respective heat treatment cycles: (*a*, *b*) Steel 1, (*c*, *d*) Steel 2, (*e*, *f*) Steel 3, and (*g*, *h*) Steel 4. γ_f thin film RA, γ_b blocky RA, α' alpha martensite, ε epsilon martensite, *FM* fresh martensite. The colors used to depict the different crystal structures in EBSD analysis are red for γ and blue for α'-martensite (Color figure online).

identified within a few γ grains, but the thin ε-martensite observed in the SEM micrograph could not be identified due to the insufficient spatial resolution of the electron microscope used. The dislocation density of the γ at room temperature was determined to be 5.7805×10^{14} m^{-2}, which is observed to be significantly lower than that of RA in Steel 1.

C. *Steel 3: Microstructure and RA (Thin Film and Block) Stability*

Dilatometer results, shown in Figure 2(c), indicate that Steel 3 was fully austenitized when heated to 900 °C and was partially transformed to martensite during the initial quenching to the quench temperature (QT) of 170 °C. The M_s temperature of the bulk γ was determined to be 255 °C ± 5 °C. Furthermore, during cooling to sub-zero temperatures (− 150 °C) from the partitioning temperature of 450 °C, no volume expansion was observed, indicating no secondary martensite formation and that the RA is stable and has a M_s temperature lower than − 150 °C.

The microstructure of Steel 3, Figure 5(e), consists of a martensitic matrix and RA. The RA is present in the form of bulky blocks with an average size of 3 μm but there is also some thin film RA between the martensite laths. Carbides were occasionally observed in the martensite. XRD measurements (Figure 3) clearly showed the presence of RA (fcc) and α'-martensite (bcc), with volume fractions of 0.24 ± 0.03 and 0.76 ± 0.03, respectively. The EBSD analysis [Figure 5(f)] confirms the XRD results and shows the RA (fcc) and α'-martensite (bcc) with a volume fraction of RA of 0.22 and martensite of 0.72. Moreover, some regions with dark contrast were identified and may correspond to fresh martensite, but since the dilatometer results did not show any volume expansion during cooling after the partitioning stage, this fresh martensite is probably deformation-induced martensite formed during sample preparation rather than martensite formed during quenching. The average carbon content of the RA is determined to be 0.54 wt pct (Table III) using XRD. It should be noted that while determining the carbon content from the RA lattice parameter it is considered that diffusion of substitutional alloying elements is negligible at the temperature involved in Q&P processing and that carbon is the only element affecting the variation in the lattice parameter. The dislocation densities of the RA and α'-martensite are determined to be 4.5274×10^{15} m^{-2} and 5.9722×10^{15} m^{-2} respectively.

Furthermore, XRD measurements of the sample quenched in LN (Figure 4) show a decrease in RA volume fraction to 0.19 ± 0.03 (Table III) and that some martensite has formed upon quenching in LN. Combined with the dilatometry result showing no secondary martensitic transformation down to − 150 °C, the M_s temperature of the RA is considered to be between − 150 °C and − 196 °C.

D. *Steel 4: Microstructure and γ (Bulk) Stability*

Dilatometer results shown in Figure 2(d) reveal that the steel is fully austenitized when heated to 900 °C. The M_s temperature of the bulk γ was determined to 170 °C ± 5 °C. This transformation is further

Table III. Quantitative Results of XRD Analysis of RA, α′-Martensite, ε-Martensite, and Average Carbon Content of γ in the Different Steels

Material	f_γ	$f_{\alpha\prime}$	f_ε	c_γ
Steel 1	0.29 ± 0.03	0.71 ± 0.03	—	0.69 ± 0.02
Steel 2	0.98 ± 0.03	—	0.02 ± 0.01	0.68 ± 0.02
Steel 3	0.24 ± 0.03	0.76 ± 0.03		0.54 ± 0.02
Steel 4	0.14 ± 0.03	0.86 ± 0.03	—	0.55 ± 0.02
Steel 1_LN	0.27 ± 0.03	0.73 ± 0.03	—	—
Steel 3_LN	0.19 ± 0.03	0.81 ± 0.03		—

confirmed by the predominantly martensitic microstructure observed in the SEM micrographs presented in Figure 5(g).

Furthermore, the XRD analysis shown in Figure 3 indicates the presence of both α′-martensite and RA in the steel with 0.86 ± 0.03 and 0.14 ± 0.03 volume fractions, respectively. The EBSD combined image quality map (IQ) and color-coded phase map in Figure 5(h) reveals mainly α′-martensite (bcc) and some RA (fcc) with volume fractions of 0.94 and 0.05, respectively. It should be noted that the relatively low volume fraction of γ observed in the EBSD and SEM micrographs compared to the XRD result is probably due to the mechanically induced transformation of RA to martensite during sample preparation. Additionally, the lower volume fraction in the EBSD images could also be attributed to some unrecognized regions that might contain very small regions of austenite, finer than the scanning step size. The dislocation density of the RA at the room temperature is determined to be 8.937×10^{15} m^{-2} and is significantly higher than the dislocation density observed in RA in Steel 3. The dislocation density of the α′-martensite is determined to be 2.729×10^{16} m^{-2}.

E. *Calculation of α′-Martensite Start Temperature*

The M_s temperatures for the four steels were calculated taking into account the composition and size of γ using the thermodynamic approach described in Reference 4, 40. The M_s temperature is calculated by determining the temperature at which the available driving force, *i.e.*, the difference in Gibbs energies between the γ and α′-martensite, ΔG^{chem}, reaches a critical driving force to overcome the barrier for the martensitic transformation.

$$\text{At } T = M_s, \quad \Delta G^{\text{chem}} = \Delta G^{*} + \Delta G^{\text{size}} \qquad [4]$$

ΔG^{chem} is dependent on the chemical composition and temperature and was calculated with the Thermo-Calc software using the TCFE6 database.[41] It should be noted that the Gibbs energy for the α′-martensite was calculated using the bcc phase including Zener ordering, which is related to the distribution of carbon atoms. The barrier for martensitic transformation (ΔG^*) was calculated as a function of the chemical composition and temperature using the empirical relations given by Stormvinter *et al.*[40] The influence of grain size is taken into account by considering it as an additional Gibbs energy barrier for the martensitic transformation.[4] Table IV presents the calculated and experimental M_s temperatures for the bulk γ and RA in the four steels. To evaluate the effect of size on the stability of γ, the average size of γ, measured from micrographs was included in the calculations. The results show that the calculated M_s temperatures agree with the experimental values within an uncertainty of ± 60 °C for the bulk γ in the four steels. However, the calculated and experimental M_s temperatures for the RA in Steels 1 and 3 differed substantially.

IV. DISCUSSION

Individual contributions of several governing factors (such as composition, size, morphology, and matrix) to the stability of RA remain unclear. This is due to the inherent difficulties in separating these factors in a multiphase microstructure to understand their direct effects on stability. To overcome this challenge, this study was designed to isolate the influence of composition and focus on the role of microstructural factors on the thermal stability of RA. This was achieved by designing the samples and their respective heat treatment processes to exclude the effect of the austenite composition and comparing the γ thermal stabilities, specifically $\gamma \rightarrow \alpha'$ M_s temperature, in four medium-Mn steels. These four steels were grouped into two pairs (Steel 1 and 2; Steel 3 and 4). Each pair consists of one two-phase microstructure and one bulk γ microstructure before final quenching, with γ of nearly the same composition, thus providing an opportunity for a comparative analysis of the γ stability. The results of this study show a substantial difference in the thermal stabilities of γ between the two microstructures in each pair. In particular, RA within the two-phase microstructures showed very high stability, with extremely low M_s temperatures of lower than − 196 °C for Steel 1 and − 150 °C for Steel 3. In contrast, their corresponding bulk γ showed no such high stability, as demonstrated by relatively high M_s temperatures of − 8 °C for Steel 2 and 170 °C for Steel 4. In the first pair, Steel 1 and Steel 2, a temperature difference of at least 170 °C was observed. In the second pair, Steel 3 and Steel 4, the temperature difference was even larger with at least 286 °C. These differences suggest a significant influence

of microstructural factors such as size and morphology of γ as well as matrix in determining the thermal stability of RA in the two-phase microstructure.

The influence of different microstructural factors on the thermal stability of RA was further evaluated through a thermodynamic-based M_s model. This model takes into account both composition and size, and its calculations were compared with experimental results to identify whether factors that are not considered in the model could influence the thermal stability. Indeed, if there were substantial differences between the experimental results and the model calculations, and more specifically between the different microstructures, it would explicitly point out factors affecting the stability. The M_s temperatures of the bulk γ for the four steels, calculated using the model, are presented in Table IV. It is worth reminding that even if the final microstructures are the result of a specific heat treatment where a two phase microstructure has been created in Steel 1 and Steel 3, they were also fully austenitic structure after austenitization for which the M_s temperature could also be measured. The calculated M_s temperatures of the bulk γ are in reasonable agreement with the measured M_s temperatures within a margin of error of $\pm$ 60 °C. This error margin is considered reasonable due to the well-established uncertainties present in the M_s measurements[39,42] and thus the thermodynamic databases used were considered to sufficiently well represent the influence of composition and size of the bulk γ.

Moreover, within the accepted error margin, it was observed that the calculated M_s temperatures for the bulk γ were lower than the measured ones for steels 1, 3 and 4, while it was higher for Steel 2. This observation that calculated temperatures being lower for three of the four steels than measured temperatures suggest a potential systematic error by the model for the current steel compositions. However, the opposite behavior shown by Steel 2 further suggests that an additional factor that is not considered in the model might have influenced its M_s temperature. During our investigation, instances of ε-martensite were observed within steel 2. This ε-martensite is considered important because it is recognized as a precursor to α'-martensite formation and, therefore influences the $\gamma \rightarrow \alpha'$ M_s temperature.[43] While ε-martensite formation could theoretically increase M_s temperature by promoting α'-martensite nucleation, here a decrease in M_s temperature is observed compared to the calculated value which did not consider the effect of ε-martensite formation. This observation could indicate that ε-martensite might in some cases have a suppressing effect on the α'-martensite transformation, contrary to what one might expect. This hypothesis, though speculative, challenges our understanding of the ε-martensite role in the transformation process and suggests that more detailed investigations of its contributions are needed.

The model, while not explicitly validated for two-phase microstructures, was also applied to the current two-phase microstructures to identify any inconsistencies and to isolate additional factors influencing the thermal stability of RA. The calculations for the two-phase microstructures of Steel 1 and Steel 3 showed significant differences in comparison to the experimental results. The influence of size on the stabilization of RA is already considered within the model, as evident from the significant decrease in M_s temperature shown in Table IV. Despite this contribution of size, it is insufficient in explaining the large decrease in M_s observed in two-phase microstructures. Moreover, it is essential to delineate possible sources that could affect the calculated M_s temperature of the RA in these two-phase microstructures. Experimental uncertainties in measurements of RA composition and size may affect the calculated M_s values, however, these uncertainties alone do not account for the observed high stability of the RA within the two-phase microstructure. This is evidenced by the data in Table IV, where the thermal stabilities of the RA in Steels 1 and 3 are seen to be considerably higher than the values calculated by the model, even after accounting for the uncertainty. It should be noted that the margin of uncertainty considered in Table IV is considerably larger than the uncertainty in the actual chemical composition. Furthermore, the model used the average composition and size, determined from the measurements, to calculate the M_s temperature. It is possible that some inhomogeneities exist, both within and among the different RA grains, along with size variations within the two-phase microstructure due to fluctuations in the process and immediate surroundings of the grains. These variations also do not influence the analysis in the current context. This is due to the fact that the M_s temperature is primarily determined by the least stable austenite within the overall microstructure. This typically refers to the austenite grains that either contain a lower-than-average composition and/or possess a larger-than-average size that has the highest M_s temperature in the microstructure. It becomes apparent that the measured M_s temperatures represent an extreme case. The exact composition as opposed to the average composition consideration would likely result in even lower M_s temperatures than the already observed decreased M_s temperature. Thus, it becomes evident that the stability of γ in a bulk microstructure can be explained by composition and grain size. However, these factors do not provide a sufficient explanation for the stability of RA in a two-phase microstructure.

It seems that there is an additional factor in explaining the high stability of the RA in the two phase microstructure which could be the surrounding matrix. The characteristics of the matrix, including composition and strength exert a variety of mechanical and thermodynamic effects on RA.[33,44] It is known that a hard matrix, such as a martensitic matrix, can increase the stability of the RA by hydrostatic pressure and resist plastic accommodation from the transformation strain.[45,46] However, in this study, we observed high thermal stability in the RA of Steel 1 and Steel 3, regardless of large differences in heat treatment leading to different strength of the matrix. Steel 1 was subjected to intercritical annealing at a relatively high temperature of 650 °C for 3 hours, substantially reducing its dislocation density to 1.0271×10^{15} m^{-2} and resulting in a relatively soft martensitic matrix due to the extended tempering process. On the other hand, Steel 3 was subjected to a brief tempering at a relatively low

Table IV. Experimental and Calculated Martensite-Start Temperatures (M_s) of the Four Steels (Bulk and RA)

Material	C	Mn	Si	Cr	Fe	Grain Size d (μm)	Exp. M_s (°C)	Calc. M_s (°C) (Without Grain Size Included)	Calc. M_s (°C) (With Grain Size Included)	ΔM_s (Difference Between Experimental and Calculated)
Steel 1										
Bulk	0.18 ± 0.02	5.08 ± 0.02	—	—	bal.	30	285	236	225	60
Retained γ	0.69 ± 0.02	7.30 ± 0.3	—	—	bal.	0.6	< LN	54*	− 26**	> 170
Steel 2										
Bulk	0.68 ± 0.02	7.31 ± 0.02	—	—	bal.	35	− 8	56*	45**	− 53
Steel 3										
Bulk	0.31 ± 0.02	4.02 ± 0.02	1.62 ± 0.02	1.01 ± 0.003	bal.	30	255	227	216	39
Retained γ	0.54 ± 0.02	4.02 ± 0.02	1.62 ± 0.02	1.01 ± 0.003	bal.	3	− 150 to LN	171*	136**	> 286
Steel 4										
Bulk	0.56 ± 0.02	4.01 ± 0.02	1.63 ± 0.02	1.01 ± 0.003	bal.	30	170	166*	155**	15

*A carbon variation of ± 0.1 wt pct C results in an effective variation of calculated M_s temperature by approximately ± 25 °C.**A grain size variation of ± 0.4 μm results in an effective variation of calculated M_s temperature by approximately ± 15 °C.

temperature of 450 °C for 3 minutes, maintaining a higher dislocation density of 4.5274×10^{15} m^{-2} and implying a harder martensitic matrix. It appears that both types of matrices, harder and softer, can contribute to high RA stabilities, suggesting that the strength of the matrix alone cannot fully explain the observed high RA stability. This raises an important question about the specific roles that hard and soft matrices play in determining RA stability. It also suggests a potential additional factor that should be considered alongside the strength of the matrix, in determining RA stability. This factor could be the strength of the austenite. In our study, we noted that the room temperature dislocation densities for RA in Steel 1 ($\rho = 2.7369 \times 10^{15}$ m^{-2}) and Steel 3 ($\rho = 5.9722 \times 10^{15}$ m^{-2}) are within an intermediate range. This range is between the low dislocation densities (~ 10^{13} to 10^{14} m^{-2}) and high densities (> 10^{16} m^{-2}), as discussed in the introduction. While the specific influence of these intermediate dislocation densities on RA stability remains to be fully understood, we observed that these densities are greater than those of their respective matrices ($\rho = 1.0271 \times 10^{15}$ m^{-2} for Steel 1 and $\rho = 4.5274 \times 10^{15}$ m^{-2} for Steel 3). However, it is important to note that they do not solely define the strength of the RA in comparison to their corresponding matrices. The RA and martensite have inherently different structures, which significantly contribute to their strength characteristics. Consequently, the higher dislocation densities of the RA can be seen as an aspect of a complex interplay between dislocations, phase characteristics, and structural attributes in determining the overall strength and stability. Therefore, in addition to dislocation densities, a comprehensive understanding of the interaction between the different structures and phases in both the RA and the matrix is crucial for determining stability.

Regarding specifically the influence of morphology, this study revealed a high stability for both film RA (γ_f) and block RA (γ_b) morphologies within the two-phase microstructures. More specifically, Steel 1 exhibited high stability for γ_f while a mixture of γ_f and γ_b in Steel 3 also indicated high stability. While these results did not highlight any significant morphological differences, the potential influence of morphology should not be ignored. It is possible that the morphology could affect the thermal stability, although the extent of any such influence requires additional research. Additionally, the role of dislocations on the stability of γ, although less noticeable in this study, is another important factor that needs further investigation. Table II shows the dislocation densities evaluated at room temperature in the current four steels for both martensite and γ at room temperature. A certain correlation is apparent between the dislocation density and the stability of RA in the Steel 1 and γ in the Steel 2 pair. It was observed that the higher dislocation density in RA in Steel 1 ($\rho = 2.7369$ 10^{15} m^{-2}), as compared to γ in Steel 2 ($\rho = 5.7805$ 10^{14} m^{-2}), corresponds with greater stability of the retained austenite. This observation aligns with the theory that an increase in dislocation density contributes

to the stability of austenite. However, the same cannot be concluded for the Steel 3 and Steel 4 pair. This is due to Steel 4 showing a higher dislocation density due to martensitic transformation during quenching from the austenitization temperature. These results provide some qualitative insights, however, the contributions of both the morphology and the dislocation density to austenite stability require more comprehensive investigation.

Moreover, the influence of the matrix extends beyond the mechanical constraints and is complex. For instance, the RA and the martensitic matrix have different coefficients of thermal expansion, which could potentially decrease the stability of the RA. Generally, γ has a higher thermal expansion coefficient than martensite, indicating that it will expand and contract more than martensite when subjected to thermal treatment. This difference in thermal expansion will result in thermal strains and stress concentrations at the interface between RA and martensite that could trigger the transformation of RA to martensite and subsequently reduce the stability of RA. However, the interplay between these competing effects and the relative importance of each factor still remains unclear.

These results form a preliminary step towards a deeper understanding of the stability of RA. This study emphasizes that factors such as morphology, dislocation density, and the matrix influence the thermal stability of RA, in addition to the composition and size, which are typically considered the primary contributors within the two-phase microstructure. Therefore, a complete understanding of these factors is crucial. Future studies should prioritize a systematic exploration of matrix characteristics, including its chemical composition, microstructure, and mechanical properties on the stability of RA. Understanding how these characteristics impact the stability of RA would be highly beneficial, and it could further provide valuable insights into their interaction with morphology and their cumulative influence on overall stability behavior. This understanding could potentially be achieved through the development of new models such as finite element method (FEM) simulations and advanced experimental techniques such as synchrotron diffraction measurements. Furthermore, this study has also revealed substantial discrepancies between the observed RA stabilities in two-phase microstructures and calculations, highlighting a gap in existing model frameworks that do not adequately consider the microstructural factors. The integration of microstructure-related factors, such as morphology, dislocation density, and matrix, into existing models can enhance the accuracy of the predictions. Such a development could significantly influence the design of advanced high-strength steels with controlled morphology, dislocation densities, and matrix interactions.

V. CONCLUSIONS

The current study investigated the thermal stability of RA in medium-Mn steels, with a particular emphasis on microstructural factors namely size, morphology, and the surrounding matrix. The following conclusions were drawn based on the findings of this investigation.

(a) The two-phase microstructures showed significantly higher thermal stability of RA compared to that of bulk γ microstructures with identical composition, signifying the critical role of microstructural factors in determining thermal stability.
(b) A thermodynamic-based M_s model was used to evaluate the influence of chemical composition and size on the thermal stability of γ. While these factors significantly contribute to γ thermal stability, they alone cannot satisfactorily account for the increased RA stability observed within the two-phase microstructure, emphasizing the importance of considering additional factors governing RA stability.
(c) Excluding the influence of the RA composition, the thermal stability of RA within two-phase microstructures is governed by a combined influence of the different microstructural factors. These microstructural factors include but are not limited to, the size and morphology of the RA, and the characteristics of the surrounding matrix.
(d) The findings of this study highlight a possible significant role of the surrounding martensitic matrix on the thermal stability of RA. The influence of the matrix is complex and multifaceted, which necessitates further investigations. Understanding these complexities can guide the development of advanced high-strength steels.

ACKNOWLEDGMENTS

This work was performed within the Competence Centre Hero-m 2i, financed by VINNOVA (the Swedish Governmental Agency for Innovation Systems), Swedish industry, and KTH Royal Institute of Technology.

FUNDING

Open access funding provided by Royal Institute of Technology.

CONFLICT OF INTEREST

The authors declare that they have no conflict of interest.

REFERENCES

1. O. Bouaziz, S. Allain, C.P. Scott, P. Cugy, and D. Barbier: *Curr. Opin. Solid State Mater. Sci.*, 2011, vol. 15, pp. 141–68.
2. P.J. Jacques: *Curr. Opin. Solid State Mater. Sci.*, 2004, vol. 8, pp. 259–65.
3. V. Savic, L. Hector, H. Singh, M. Paramasuwom, U. Basu, A. Basudhar, and N. Stander: *SAE Int. J. Mater. Manuf.*, 2018, vol. 11, pp. 303–13.
4. F. Huyan: Computational Materials Design of Medium Mn Steels. Doctoral dissertation, KTH Royal Institute of Technology, Stockholm, 2018.
5. L. Liu, B.B. He, G.J. Cheng, H.W. Yen, and M.X. Huang: *Scripta Mater.*, 2018, vol. 150, pp. 1–6.
6. X. Zhang, R. Teng, T. Liu, Y. Shi, Z. Lv, Q. Zhou, X. Wang, Y. Wang, H. Liu, and Z. Xing: *Mater Charact.*, 2022, vol. 184, pp. 1–11.
7. J. Li, Y. Xu, B. Lu, Y. Yu, Y. Jing, and W. Sun: *J. Mater. Res. Technol.*, 2022, vol. 18, pp. 352–69.
8. H. Guo, Q. Li, Y. Fan, and X. Feng: *J. Mater. Res. Technol.*, 2020, vol. 9, pp. 9206–18.
9. S.M. Hasan, M. Ghosh, D. Chakrabarti, and S.B. Singh: *Mater. Sci. Eng. A*, 2020, vol. 771, pp. 1–12.
10. P. Jacques, Q. Furnémont, A. Mertens, and F. Delannay: *Philos. Mag. A*, 2001, vol. 81, pp. 1789–812.
11. S.M. Hasan, A. Mandal, S.B. Singh, and D. Chakrabarti: *Mater. Sci. Eng. A*, 2019, vol. 751, pp. 142–53.
12. B. He: *Materials (Basel)*, 2020, vol. 13, pp. 1–31.
13. J. Hu, X. Li, Q. Meng, L. Wang, Y. Li, and W. Xu: *Mater. Sci. Eng. A*, 2022, vol. 855, pp. 1–11.
14. X.C. Xiong, B. Chen, M.X. Huang, J.F. Wang, and L. Wang: *Scripta Mater.*, 2013, vol. 68, pp. 321–24.
15. J. Huang and Z. Xu: *Mater. Sci. Eng. A*, 2006, vol. 438–440, pp. 254–57.
16. D.P. Koistinen and R.E. Marburger: *Acta Metall.*, 1959, vol. 7, pp. 59–60.
17. T. Hanamura, S. Torizuka, S. Tamura, S. Enokida, and H. Takechi: *ISIJ Int.*, 2013, vol. 53, pp. 2218–25.
18. S. Takaki, K. Fukunaga, J. Syarif, and T. Tsuchiyama: *Mater. Trans.*, 2004, vol. 45, pp. 2245–51.
19. P.J. Brofman and G.S. Ansell: *Metall. Trans. A*, 1983, vol. 14A, pp. 1929–31.
20. M. Umemoto and W.S. Owen: *Metall. Mater. Trans. B*, 1974, vol. 5B, pp. 2041–046.
21. S.M.C. van Bohemen and L. Morsdorf: *Acta Mater.*, 2017, vol. 125, pp. 401–15.
22. C. Celada-Casero, J. Sietsma, and M.J. Santofimia: *Mater. Des.*, 2019, vol. 167, p. 107625.
23. H.S. Yang and H.K.D.H. Bhadeshia: *Scripta Mater.*, 2009, vol. 60, pp. 493–95.
24. A. Arlazarov, M. Gouné, O. Bouaziz, and A. Hazotte: *Philos. Mag. Lett.*, 2017, vol. 97, pp. 125–31.
25. S. Morito, H. Yoshida, T. Maki, and X. Huang: *Mater. Sci. Eng. A*, 2006, vol. 438–440, pp. 237–40.
26. E. Jimenez-Melero, N.H. van Dijk, L. Zhao, J. Sietsma, S.E. Offerman, J.P. Wright, and S. van der Zwaag: *Scripta Mater.*, 2007, vol. 56, pp. 421–24.
27. G.B. Olson and M. Cohen: *J. Less-Common Met.*, 1972, vol. 28, pp. 107–18.
28. F.G. Caballero, C. García-Mateo, J. Chao, M.J. Santofimia, C. Capdevila, and C.G. De Andrés: *ISIJ Int.*, 2008, vol. 48, pp. 1256–62.
29. S.H. He, B.B. He, K.Y. Zhu, R. Ding, H. Chen, and M.X. Huang: *Scripta Mater.*, 2019, vol. 168, pp. 23–27.
30. J. Chiang, J.D. Boyd, and A.K. Pilkey: *Mater. Sci. Eng. A*, 2015, vol. 638, pp. 132–42.
31. J. Chiang, B. Lawrence, J.D. Boyd, and A.K. Pilkey: *Mater. Sci. Eng. A*, 2011, vol. 528, pp. 4516–21.
32. D. De Knijf, C. Föjer, L.A.I. Kestens, and R. Petrov: *Mater. Sci. Eng. A*, 2015, vol. 638, pp. 219–27.
33. I.B. Timokhina, P.D. Hodgson, and E.V. Pereloma: *Metall. Mater. Trans. A*, 2004, vol. 35A, pp. 2331–41.
34. B.D. Cullity: *Elements of X-ray Diffraction*, Addison-Wesley Publishing, Reading, 1956.
35. L. Cheng, A. Böttger, T.H. de Keijser, and E.J. Mittemeijer: *Scripta Metall. Mater.*, 1990, vol. 24, pp. 509–14.
36. D.J. Dyson and B. Holmes: *J. Iron Steel Inst.*, 1970, vol. 208, pp. 469–74.
37. N.H. Van Dijk, A.M. Butt, L. Zhao, J. Sietsma, S.E. Offerman, J.P. Wright, and S. Van Der Zwaag: *Acta Mater.*, 2005, vol. 53, pp. 5439–47.
38. G.K. Williamson and R.E. Smallman: *Philos. Mag. A*, 1956, vol. 1, pp. 34–46.
39. H.S. Yang and H.K.D.H. Bhadeshia: *Mater. Sci. Technol.*, 2007, vol. 23, pp. 556–60.
40. A. Stormvinter, A. Borgenstam, and J. Agren: *Metall. Mater. Trans. A*, 2012, vol. 43A, pp. 3870–79.
41. J.O. Andersson, T. Helander, L. Höglund, P. Shi, and B. Sundman: *Calphad*, 2002, vol. 26, pp. 273–312.
42. G.B. Olson, K. Tsuzaki, and M. Cohen: *MRS Proc.*, 1985, vol. 57, pp. 129–48.
43. Q. Gu, J. Van Humbeeck, and L. Delaey: *J. Phys. IV JP*, 1994, vol. 4, pp. 135–44.
44. E. Pereloma, A. Gazder, and I. Timokhina: *Encyclopedia of Iron, Steel, and Their Alloys*, CRC Press, Boca Raton, 2016, pp. 3088–103.
45. S.V. Radcliffe and M. Schatz: *Acta Metall.*, 1962, vol. 10, pp. 201–07.
46. K.I. Sugimoto, M. Misu, M. Kobayashi, and H. Shirasawa: *ISIJ Int.*, 1993, vol. 33, pp. 775–82.